Electronic Supplementary Material (ESI) for Organic & Biomolecular Chemistry.

Neutral rhodol-based dyes expressing localization in mitochondria

Electronic Supplementary Information

Ilaria Ferraboschi,[a‡] Juraj Ovčar,[b,c‡] Kateryna V. Vygranenko,[d] Shupei Yu,[e] Alfonso Minervino,[e], Antoni Wrzosek,[f] Adam Szewczyk, [f] Riccardo Rozza,[c] Alessandra Magistrato,[c] Kevin D. Belfield,[e] Daniel T. Gryko,[d] Luca Grisanti,[*b,c] Cristina Sissa[*a]

[a] *Department of Chemistry, Life Sciences and Environmental Sustainability, University of Parma, 43124 Parma, Italy.*

[b] *Ruđer Bošković Institute, Bijenička cesta 54, 10000 Zagreb, Croatia.*

[c] *National Research Council - Materials Foundry Institute (CNR-IOM) c/o SISSA (International School for Advanced Studies), Via Bonomea 265, 34136 Trieste, Italy*

[d] *Institute of Organic Chemistry, Polish Academy of Sciences, Kasprzaka 44/52, 01-224 Warsaw, Poland.*

[e] *Department of Chemistry and Environmental Science, College of Science and Liberal Arts, New Jersey Institute of Technology, Newark, New Jersey 07102, United States.*

[f] *Nencki Institute of Experimental Biology of Polish Academy of Sciences, Pasteura 3, 02-093 Warsaw, Poland*

‡ I.F. and J.O. are equal contributors to this work and designated as co-first authors.

Contents

List of Figures

List of Tables

S1 Computational (DFT and TDDFT) study

S1.1 Computational details

Density Functional Theory (DFT) simulations were run using the `Orca 5.0.2` package [S1]. PBE0 functional [S2] with def2-TZVP basis set [S3] in its default DFT implementation (with `RI-J` integral approximation scheme and use of def2-J auxiliary basis set [S4]). Molecules were prepared and optimised in different environments: vacuum or implicit continuum solvation using CPCM-SMD model [S5] for DCM, DMSO and water solvents. Each of these ground state (S_0) geometry relaxation was followed by a frequency calculations. At this geometries time-dependent DFT (TDDFT) transition energies were evaluated consistently to simulate electronic absorption energies in vacuum or implicit solvents, as well as to describe transition dipole moments. Similarly, the first excited state (S_1) was optimised with TDDFT and from its relaxed geometry we evaluated the emission properties (energies and transition dipole). Due to the various internal rotations, for optimisation calculations (performed using the BFGS algorithm), extra-care had to be taken in order to avoid non-negative frequencies.

S1.2 Geometry analysis

Geometrical information were extracted from S_0 and S_1 optimised geometries. For convenience, for each molecules we defined two dihedral angles to account for their geometry (for both ground and excited states):

θ is the inter-ring torsional angle, expressing the angle formed by three rings and the upper aromatic ring (see Fig. S1 (a));

σ is the torsional angle expressing the out-of-plane behaviour of the sulfone group (see Fig. S1 (b)).

Additionally, we collected information about the angle, labeled as γ, formed between the dipole moment and the reference orientation of the long axis of the 3-rings moiety, selected as the vector connecting atoms N-O (see figure S2 for its definition). The considered dipole moment is either the transition dipole moment (computed from TDDFT) μ_t or the ground or excited state dipole moment, μ_G or μ_{S1}, respectively. The full list of both geometrical and dipole angles is reported in Table S2 (ground state geometries) and Table S3 (first excited state geometries).

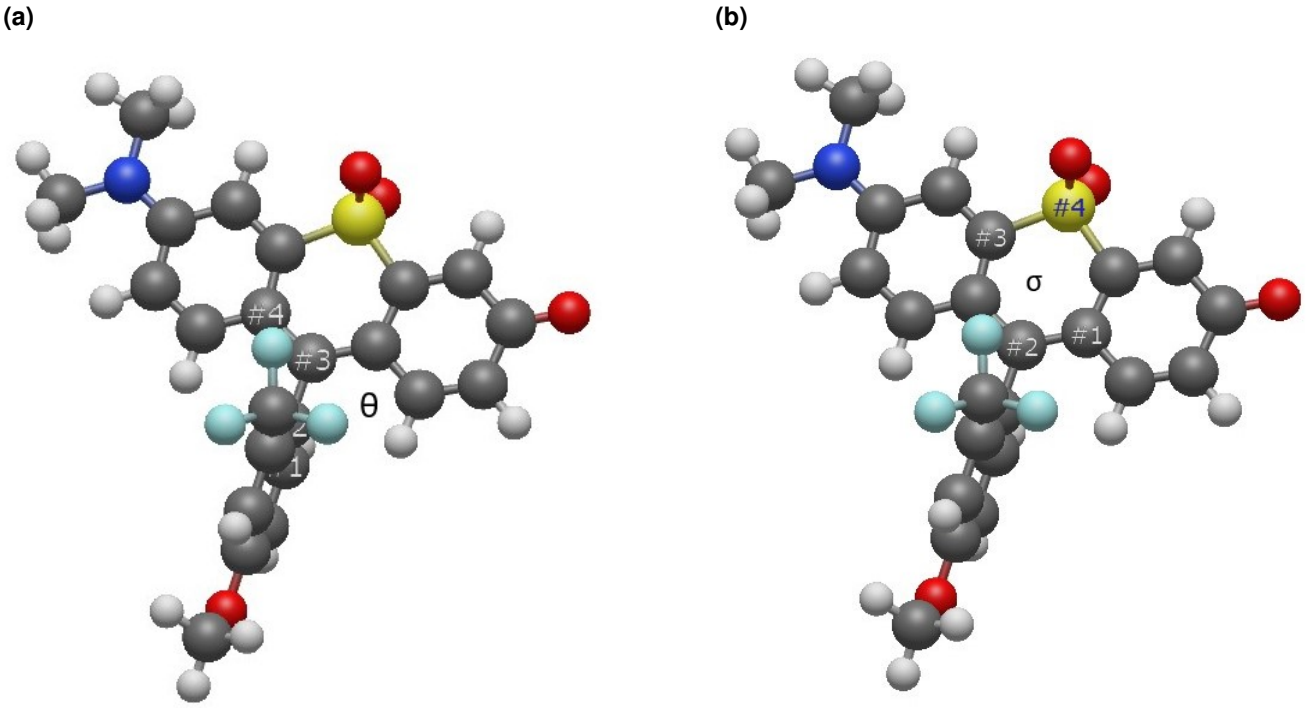

Figure S1 (a) Definition of the θ dihedral through four atoms. **(b)** Definition of the σ dihedral through four atoms. As an example, the sketch is made on the ground state structure of **MOFM** in water.

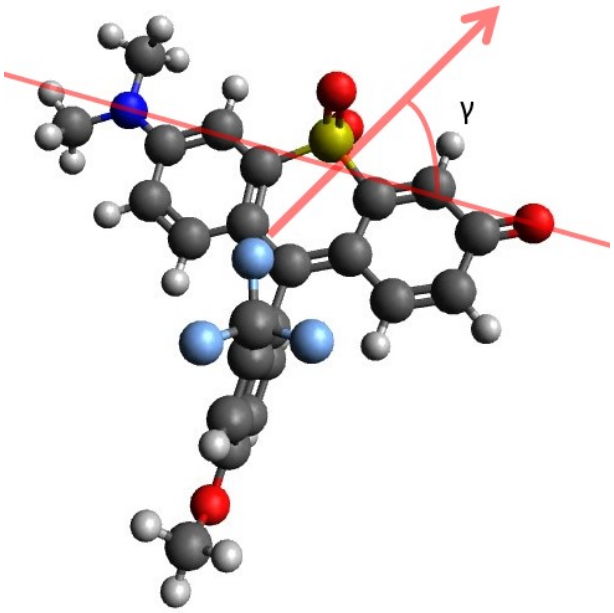

Figure S2 Definition of the γ angle, formed by the dipole moment (marked with an arrow) with respect to the N-O vector. As an example, the sketch is made on the ground state structure of **MOFM** in water.

S1.3 DFT and TDDFT detailed results

Table S1 Ground state dipole moments (in Debye) of **FM** and **MOFM** in different solvents, calculated using the electronic density obtained with PBE0 (μ_ρ), Mulliken (μ_M) and Loewdin charges (μ_L)

Molecule	Solvent	μ_ρ	μ_M	μ_L
FM	Vacuum	12.346	13.253	8.604
	Water	22.918	23.084	18.197
MOFM	Vacuum	12.638	13.716	9.318
	Water	23.211	23.492	18.870

Table S2 Optimised ground state (S_0) geometrical properties and ground state dipole orientation from DFT PBE0/def2-TZVP simulation, as well as transition dipole moment from TDDFT (at the same geometry) - relevant for absorption. SMD continuum model was employed for DFT and TDDFT to model solvent environment. Angles are defined in S1.2. Please note that $S1$ in vacuum is an electronic state with a different character (values in parenthesis)

System	Solvent	θ (deg.)	σ (deg.)	$\gamma(\mu_G)$ (deg.)	$\lvert\mu_G\rvert$ (a.u.)	$\gamma(\mu_t)$ (deg.)	$\lvert\mu_t\rvert$ (a.u.)
FM	Vacuum	84.816	-1.086	33.03421	4.85704	(22.32015)	(0.023)
	DCM	84.540	-1.673	29.56650	7.41693	4.14178	4.182
	DMSO	84.379	-1.722	28.72791	7.76993	4.41652	4.174
	Water	84.005	-2.008	27.84176	9.01635	4.01323	4.266
MOFM	Vacuum	97.965	-1.263	37.22466	4.97193	(109.57535)	(0.055)
	DCM	84.382	-1.538	31.30542	7.59079	4.06362	4.149
	DMSO	84.362	-1.450	30.35885	7.92321	4.37406	4.209
	Water	84.784	-1.382	29.05259	9.13167	4.04960	4.228

Table S3 Optimised first-excited state (S_1) geometrical properties, excited state dipole moment and transition dipole moments from TD DFT PBE0/def2-TZVP simulation. Dipole moments are computed at the same excited state geometry and they are therefore valid for emission. SMD continuum model was employed for DFT and TDDFT to model solvent environment. Angles are defined in S1.2

System	Solvent	θ (deg.)	σ (deg.)	$\gamma(\mu_{S1})$ (deg.)	$\lvert\mu_{S1}\rvert$ (a.u.)	$\gamma(\mu_t)$ (deg.)	$\lvert\mu_t\rvert$ (a.u.)
FM	Vacuum	87.131	-16.153	44.68224	3.59677	2.95181	0.095
	DCM	88.560	-23.929	33.58831	7.28955	4.47945	3.843
	DMSO	88.064	-23.527	32.46300	7.69891	4.73807	3.913
	Water	88.205	-23.487	30.94450	8.89998	4.35154	3.97
MOFM	Vacuum	89.502	16.904	43.12471	3.50808	3.02476	0.131
	DCM	89.156	-1.165	31.95234	7.75051	3.69744	4.176
	DMSO	89.094	-1.679	30.82020	8.12510	3.99346	4.212
	Water	89.175	13.986	25.56076	10.12986	3.11130	4.877

Table S4 TDDFT absorption transition energies and oscillator strengths towards the first two excited states (at the relevant ground state geometries). SMD continuum model was employed for the solvent environment.

			$S_0 \rightarrow S_1$			$S_0 \rightarrow S_2$		
		ω_{exp} (eV)	ω (eV)	Osc. strength	Major MO contr.	ω (eV)	Osc. strength	Major MO contr.
FM	Vacuum		2.60	0.00003	H-1→L : 96%	2.94	0.8137	H→L : 89%
	DCM	2.15	2.55	1.094	H→L : 94%	2.80	0.00010	H-1→L : 96%
	DMSO	2.05	2.55	1.106	H→L : 94%	2.81	0.00007	H-1→L : 96%
	Water	1.85	2.51	1.129	H→L : 94%	3.01	0.00019	H-2→L : 91%
MOFM	Vacuum		2.64	0.00019	H-1→L : 94%	2.94	0.8155	H→L : 89%
	DCM	2.16	2.57	1.084	H→L : 94%	2.80	0.00071	H-1→L : 29%, H-2→L : 68%
	DMSO	2.06	2.56	1.093	H→L : 94%	2.80	0.00096	H-1→L : 33%, H-2→L : 64%
	Water	1.86	2.52	1.104	H→L : 94%	2.81	0.00397	H-1→L : 95%

Table S5 TDDFT emission transition energies and oscillator strengths from the first excited state to the ground state (at the relevant S_1 geometries). SMD continuum model was employed for the solvent environment.

			$S_1 \rightarrow S_0$	
		ω_{exp} (eV)	ω (eV)	Osc. strength
FM	Vacuum		2.10	0.00002
	DCM	1.82	2.12	0.9980
	DMSO	1.77	2.07	1.068
	Water	1.73	1.96	1.112
MOFM	Vacuum		2.11	0.000003
	DCM	1.82	2.23	1.208
	DMSO	1.78	2.16	1.257
	Water	1.73	2.04	1.271

S1.4 Molecular orbitals

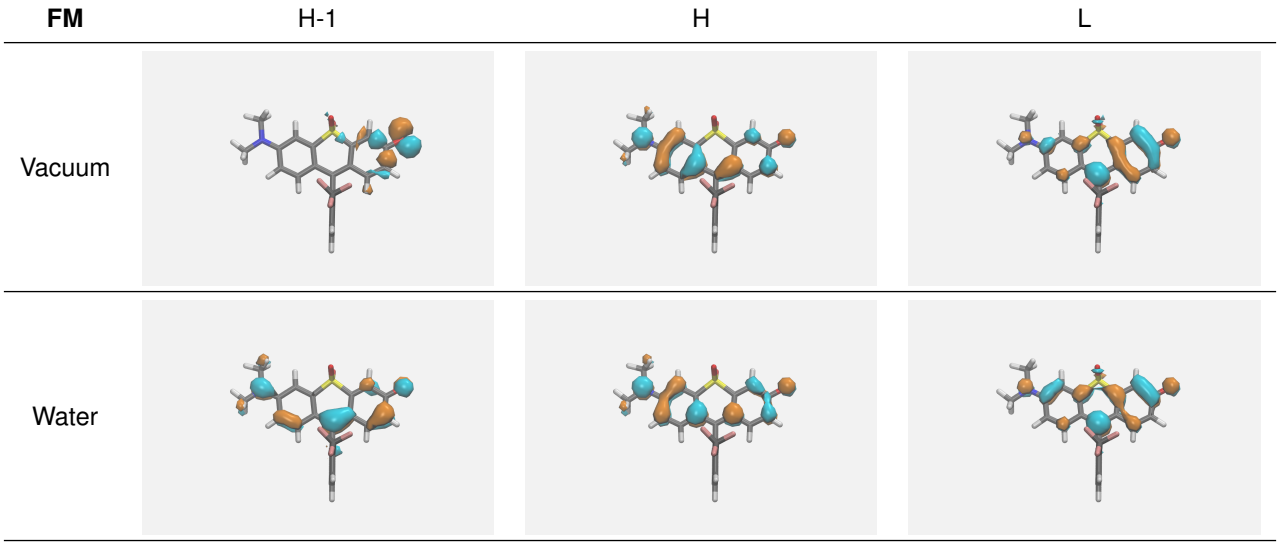

Figure S3 Frontier molecular orbitals of **FM** at ground state optimised geometries in vacuum and water. The character of HOMO (H) and LUMO (L) is conserved.

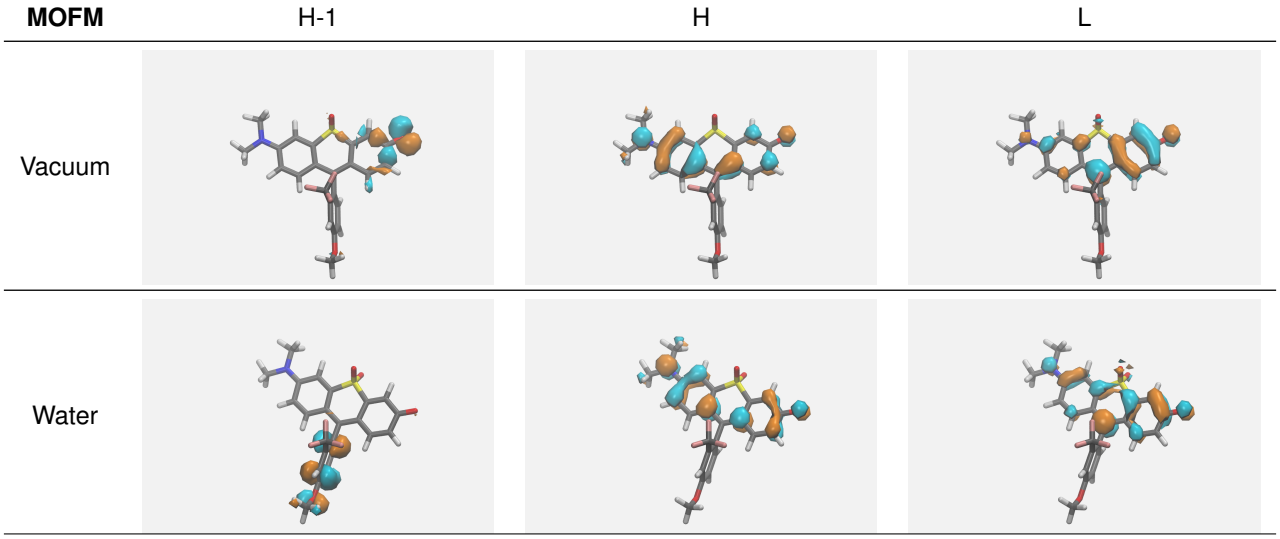

Figure S4 Frontier molecular orbitals of **MOFM** at ground state optimised geometries in vacuum and water. The character of HOMO (H) and LUMO (L) is conserved.

S2 Detailed spectroscopic characterization of FM and MOFM

UV-vis absorption spectra were recorded with a Tecan Infinite M200 PRO plate reader or a PerkinElmer Lambda650 spectrophotometers, in 1 cm path length cuvettes.

Fluorescence emission spectra were measured using an Edinburgh FLS980 or an Edinburgh FLS1000 fluorometers on solutions with absorbance < 0.1 in 1 cm path length cuvettes.

Two-photon absorption cross sections of **FM** and **MOFM** in dichloromethane (DCM) were obtained by comparing their two-photon excited fluorescence (TPEF) intensity to that of a reference, a $1.24 \cdot 10^{-5}$ M (for **FM**) and a $1.09 \cdot 10^{-5}$ M (for **MOFM**) solution of Nile Red in DMSO, following a procedure described in the literature [S6][S7].

The experimental setup consists of a Nikon A1R MP+ multiphoton upright microscope equipped with a Coherent Chameleon Discovery femtosecond pulsed laser (≈ 100 fs pulse duration with 80 MHz repetition rate and a tunable excitation range of 700–1300 nm). A $25\times$ water dipping objective with a numerical aperture of 1.1 and 2 mm working distance was employed for focusing the excitation beam and for collecting the TPEF. The TPEF signal was directed by a dichroic mirror to a high sensitivity photomultiplier GaAsP detector, connected to the microscope through an optical fiber and preceded by a dispersive element. This detector allowed the acquisition of the TPEF signal emission spectrum (wavelength range of 430 to 650 nm), with a bandwidth of 10 nm. The correction for the wavelength dependent sensitivity of the detector was applied. The measurements were carried out using 1 cm quartz cells placed horizontally under the microscope objective. Distilled water was employed to dip the objective and the focal point was moved as close as possible to the upper cuvette wall, maximizing the signal intensity for each sample. The concentrations of the sample solutions were $1.20 \cdot 10^{-5}$ M and $1.16 \cdot 10^{-5}$ M for **FM** and **MOFM**, respectively.

Due to the limited range of the microscope detector, the emission spectra of **FM**, **MOFM** and the reference were only partially acquired. Nevertheless, in the acquired range the spectra were superimposable with the ones acquired with the fluorometers, confirming that the emitting state is the same for one- and two- photon excited fluorescence. Moreover, the TPEF integrated signal was multiplied for a correction factor accounting for the ratio between the integrated areas measured with the microscope and the fluorometer, respectively. Therefore, for each sample and for the reference, we assumed the same fluorescence quantum yield for one- and two-photon excited fluorescence. Following the procedure reported in the literature, the two- photon absorption (TPA) cross section of the sample ($\sigma_{2,\text{new}}$) as a function of the excitation wavelength λ can be obtained as [S8]:

$$\sigma_{2,\text{new}}(\lambda) = \frac{\phi_{\text{ref}}}{\phi_{\text{new}}} \frac{C_{\text{ref}}}{C_{\text{new}}} \frac{P(\lambda)^2_{\text{ref}}}{P(\lambda)^2_{\text{new}}} \frac{F(\lambda)_{\text{new}}}{F(\lambda)_{\text{ref}}} \frac{n_{\text{ref}}}{n_{\text{new}}} \sigma_{2,\text{ref}}(\lambda). \tag{S1}$$

where $\sigma_{2,\text{ref}}$ is the TPA cross section of the reference, ϕ is the fluorophore quantum yield, C is the solution concentration, n is the refractive index, $P(\lambda)$ is the laser power at wavelength λ, and $F(\lambda)$ is the integral of the TPEF spectrum, evaluated after correcting the emission spectrum for the detector sensitivity. The subscripts "new" and "ref" refer to the sample and to the reference, respectively. The absolute values of $\sigma_{2,\text{ref}}(\lambda)$ of Nile Red in DMSO were calculated using the same procedure using rhodamineB in methanol as reference ($\sigma_{2,\text{rhodamineB}}(\lambda)$ taken from the literature [S9]). TPA cross sections are expressed in Goeppert-Mayer units: $1\text{GM} = 1050$ cm^{4}s photon^{-1}.

Table S6 Quantum yields (QY) and the positions of the maxima of the absorption ($\lambda^{\text{max}}_{\text{abs}}$) and emission ($\lambda^{\text{max}}_{\text{em}}$) spectra of **FM** and **MOFM** measured in various solutions

Compound	Solvent	QY	$\lambda^{\text{max}}_{\text{abs}}$ (nm)	$\lambda^{\text{max}}_{\text{em}}$ (nm)
FM	Toluene	0.05	548	642
	DCM	0.46	576	680
	DMSO	0.28	605	699
	PBS	0.04	669	717
	Cell medium	0.01	669	717
MOFM	Toluene	0.06	548	647
	DCM	0.45	574	680
	DMSO	0.30	601	698
	PBS	0.02	668	717
	Cell medium	0.01	669	717

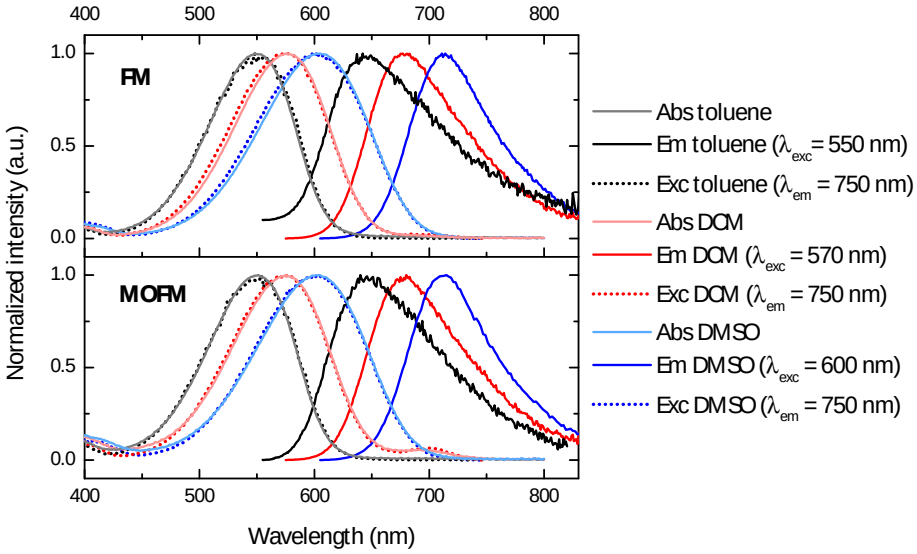

Figure S5 Absorption (Abs), emission (Em) and excitation (Exc) spectra of **FM** and **MOFM** in toluene, DCM and DMSO

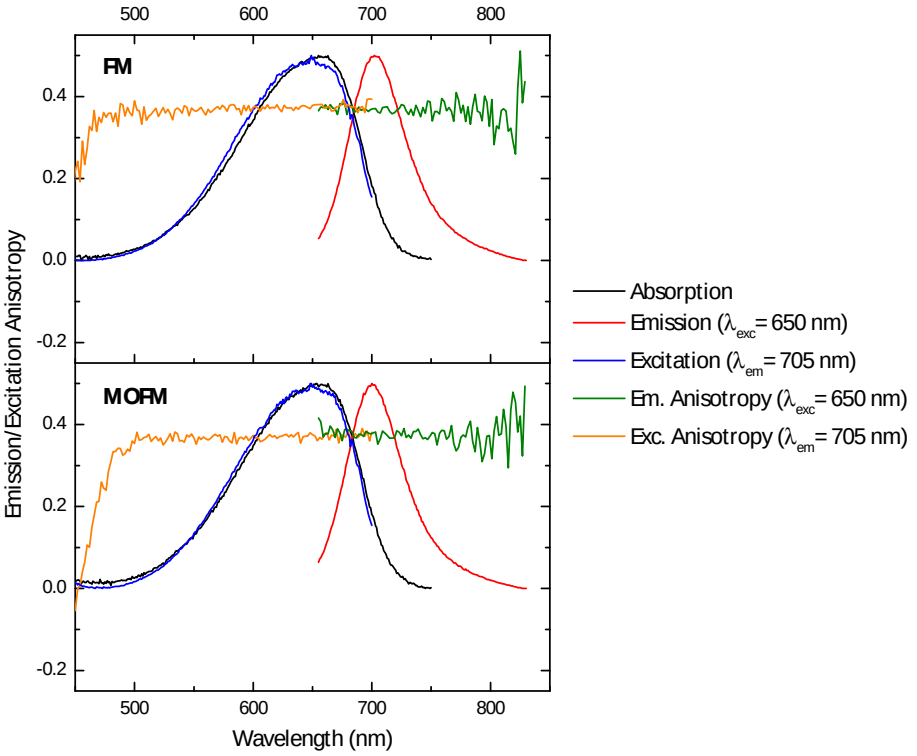

Figure S6 Absorption, emission and excitation spectra; emission and excitation anisotropy acquired in glycerol of **FM** and **MOFM**.

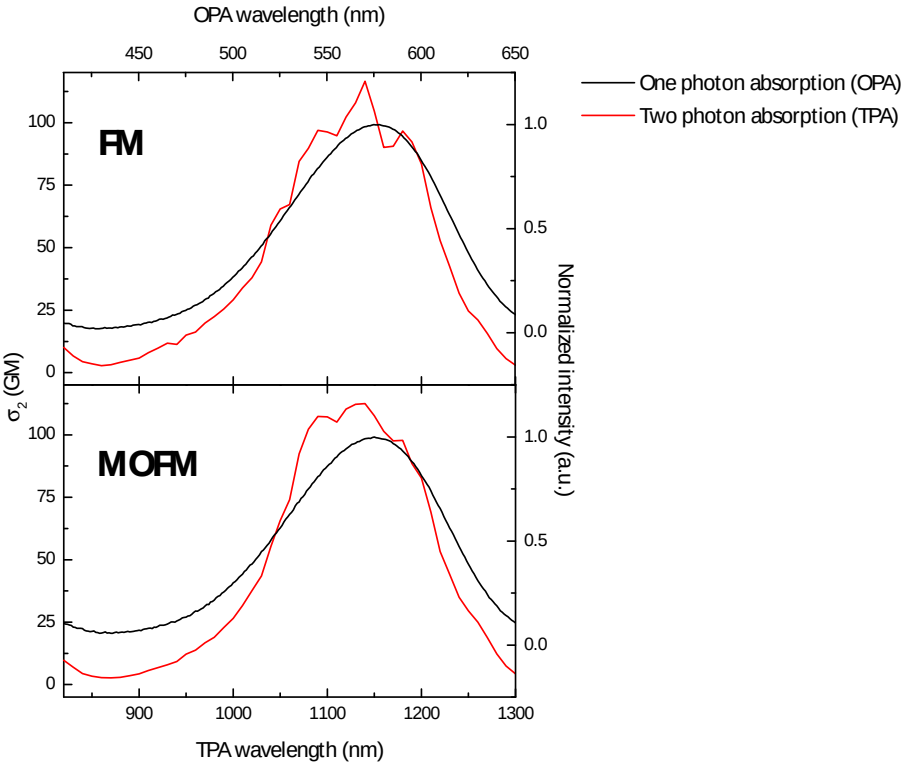

Figure S7 Normalized one-photon absorption (black lines), and two-photon absorption cross-section (red lines) of **FM** and **MOFM** in DCM.

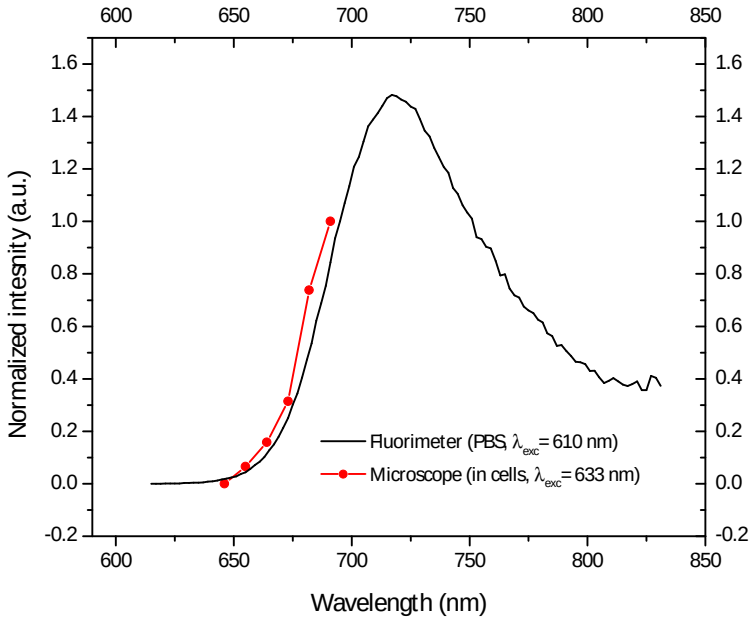

Figure S8 Emission spectra of **MOFM** in cells (red line) acquired with a confocal microscope and in PBS solution (black line) acquired with a fluorimeter.

S3 Cell viability experiments

To assess the cytotoxicity of **FM** and **MOFM**, HeLa cells were cultured in the Dulbecco's Modified Eagle Medium (DMEM) supplemented with 10% fetal bovine serum, 1% penicillin/streptomycin at 37 ℃ in a humidified 5% CO_2. Cells were placed in 96 well plates and incubated until there are no fewer than $5 \cdot 10^3$ cells per well for the experiments. Next, cells were incubated with different concentrations of **FM** and **MOFM** (0.25, 0.5, 1, 2.5, 5, 10, 20 and 40 μM). After $22\,\mathrm{h}$ of incubation, the cell culture medium was replaced with a fresh one into each well and then 20 μL of the Cell Titer 96 Aqueous One solution reagent (for MTS assay) was added into each well, followed by further incubation for 2 h at 37 ℃. The respective absorbance values were read on a Tecan Infinite M200 PRO plate reader spectrometer at 490 nm. Cell viabilities were calculated based on the following equation:

$$\text{Cell viability}(\%) = \frac{\text{Abs}^{S}_{490\text{ nm}} - \text{Abs}^{D}_{490\text{ nm}}}{\text{Abs}^{C}_{490\text{ nm}} - \text{Abs}^{D2}_{490\text{ nm}}} \cdot 100\%, \tag{S2}$$

where $\text{Abs}^{S}_{490\text{ nm}}$ is the absorbance of the cells incubated with different concentrations of experimental probe solutions, $\text{Abs}^{D}_{490\text{ nm}}$ is the absorbance of cell-free well containing only **FM** and **MOFM** at the concentration that was studied, $\text{Abs}^{C}_{490\text{ nm}}$ is the absorbance of cells alone incubated in the medium and $\text{Abs}^{D2}_{490\text{ nm}}$ is the absorbance of the cell-free well.

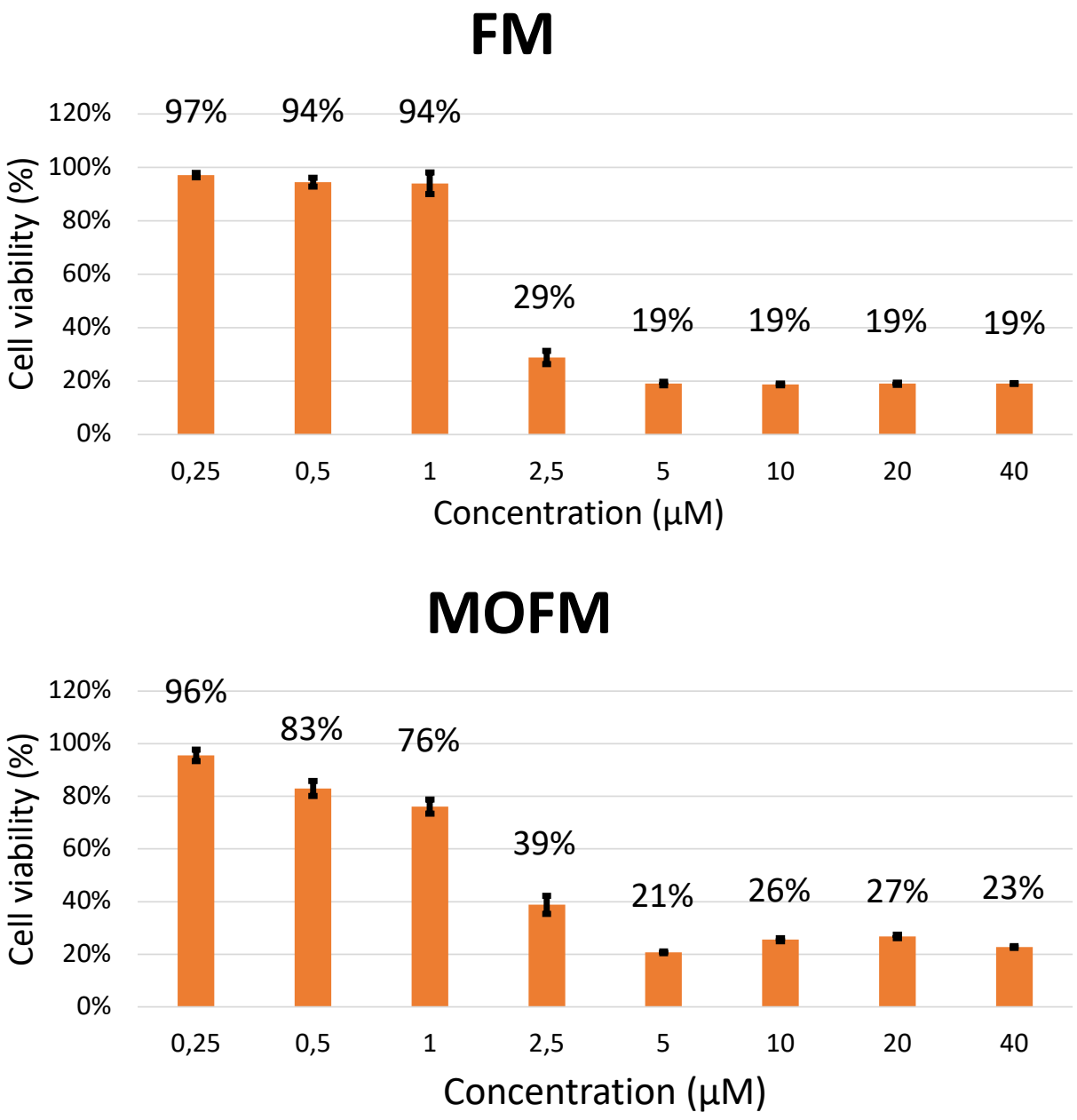

Figure S9 Cell viability after 24 hours incubation with **FM** (upper panel) and **MOFM** (lower panel).

S4 Confocal microscopy and co-localization experiments

To investigate the efficiency and specificity of compound **FM** and **MOFM**, Hela cells were employed. All cells were seeded on confocal dish (MatTek) at the density of $4 \cdot 10^4$ cells per dish and incubated for 24 h at 37 ℃. Stock solutions of **FM** and **MOFM** dissolved in DMSO were prepared at a nominal concentration of 1 mM respectively. The stock solutions were diluted to 1.5 μM with DMEM cell medium respectively and freshly placed over cells for a 30 min incubation period. Cells were washed three times with PBS and further incubated with MitotrackerTM Green FM (working concentration: 100 nM) or Lysotracker Green (working concentration: 75 nM) before cell imaging. Cells were then washed with PBS three times, and then the live cell imaging solution (Molecular Probes) was added to confocal dishes. Fluorescence images were obtained using a Zeiss LSM 780 confocal microscope (**FM** and **MOFM** Ex: 633 nm, Em: 645-750 nm. MitotrackerTM Green FM Ex: 488 nm; Em: 495-550 nm. LysotrackerTM Green Ex: 488 nm; Em: Em: 495-550 nm). Pearson's correlation coefficients were determined using ImageJ.

(a) **FM**

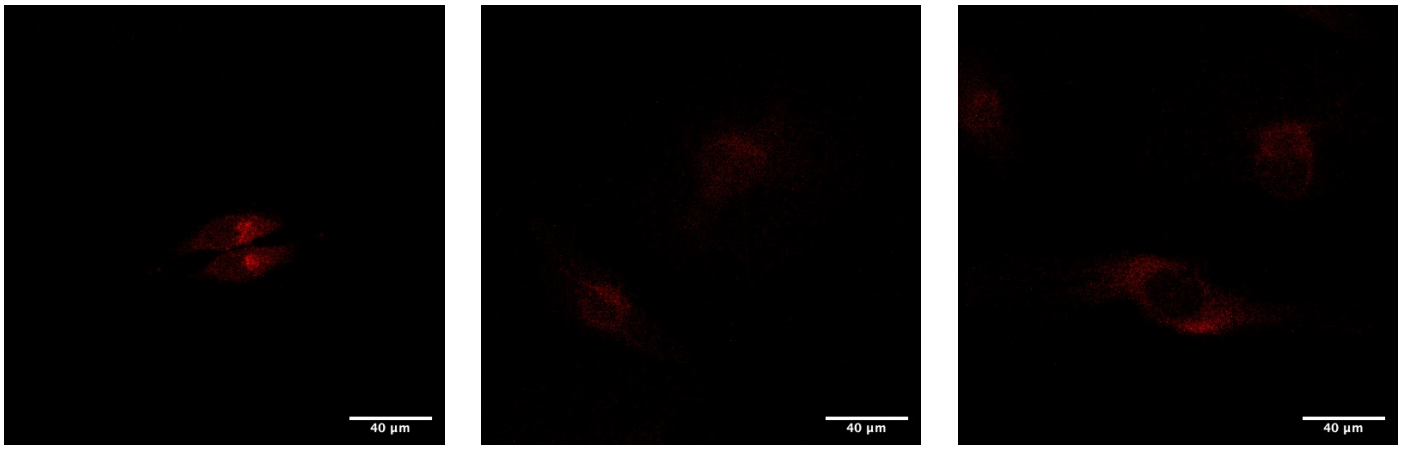

(b) **MOFM**

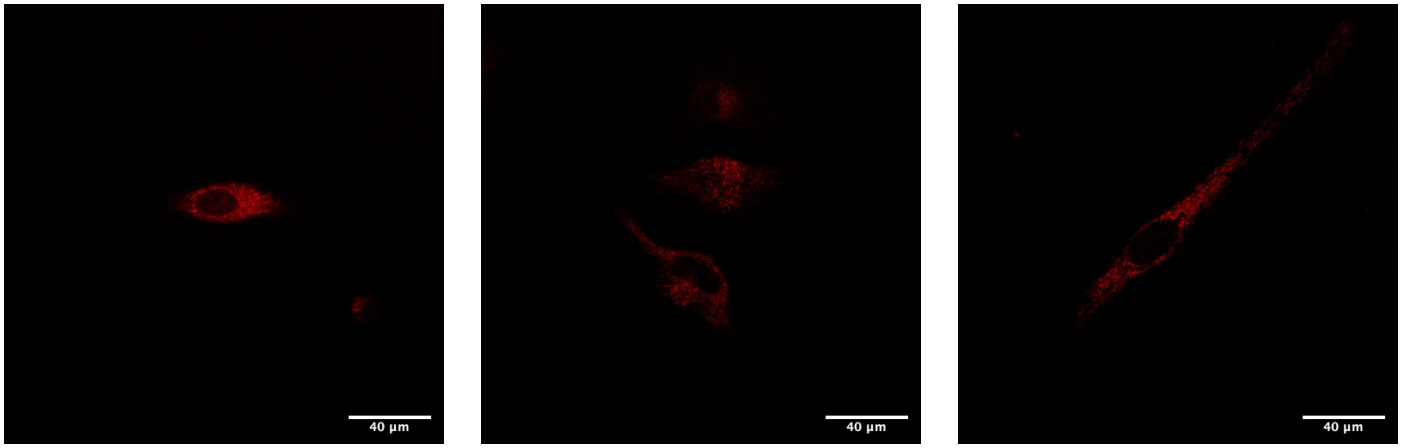

Figure S10 Images of cells after 30 minutes of incubation with (a) **FM** and (b) **MOFM**, using a concentration of 1.5 μM, an excitation wavelength of 561 nm and a detectable range of 600-750 nm. Scale bar: 40 μm.

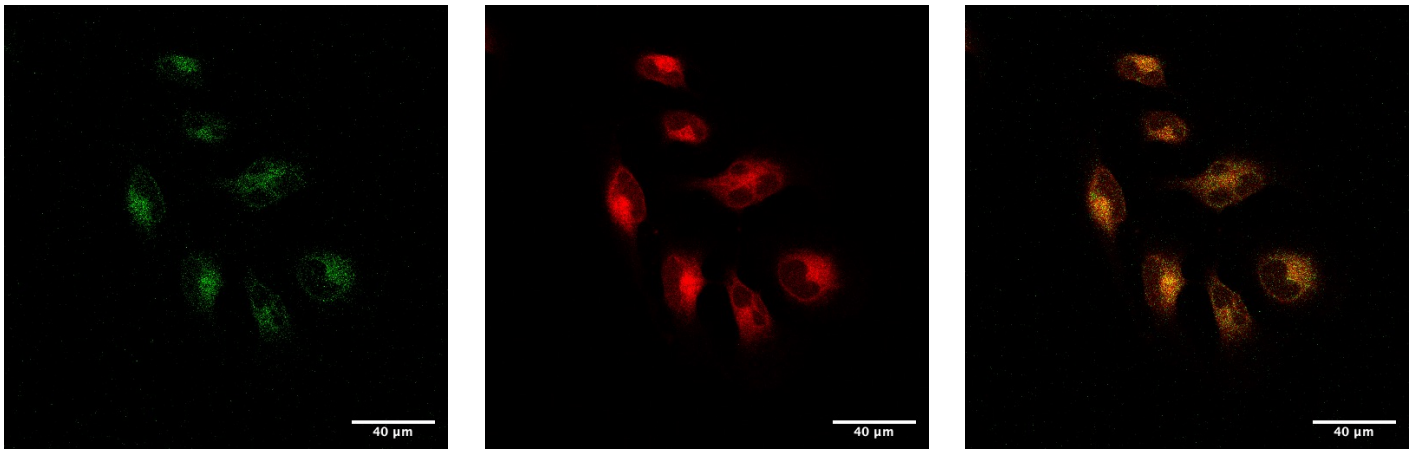

Figure S11 Co-localization of **FM** with Lysotracker Green in HeLa cells. The left panel shows the Lysotracker Green image, the middle panel shows **FM** image, with the merged image being shown on the right panel. Scale bar: 40 μm.

S5 Mitochondrial localization of cationic trackers

The main physical mechanisms of cationic tracker localization are well known. According to the chemiosmotic hypothesis, $\Delta\mu_{\mathsf{H}^+}$ is given as [S10]

$$\Delta\mu_{\mathsf{H}^+} = F\Delta\Psi_{\mathsf{NP}} + RT\ln\frac{[\mathsf{H}^+]_{\mathsf{N}}}{[\mathsf{H}^+]_{\mathsf{P}}}, \tag{S3}$$

where N denotes the mitochondrial matrix, P denotes the intermembrane space, $\Delta\Psi_{\mathsf{NP}}$ is the electrostatic potential of N relative to P, $[\mathsf{H}^+]_{\mathsf{X}}$ is the proton concentration at X, T is the temperature, F is the Faraday constant and R is the gas constant. Note that, since $[\mathsf{H}^+]_{\mathsf{P}} > [\mathsf{H}^+]_{\mathsf{N}}$, the electrostatic potential is negative, i.e. $\Delta\Psi_{\mathsf{NP}} < 0$, with typical reported values of $|\Delta\Psi_{\mathsf{NP}}|$ in isolated mitochondria being $|\Delta\Psi_{\mathsf{NP}}| \approx 150\text{-}180$ mV [S11,12]. Cationic trackers take advantage of the negative $\Delta\Psi_{\mathsf{NP}}$, accumulating in the mitochondrial matrix according to the Nernst equation, which is, in its simplest form [S13]:

$$\Delta\Psi_{\mathsf{NP}} = -\frac{RT}{zF}\ln\frac{[C]_N}{[C]_P}, \tag{S4}$$

where z is the cation's valency and $[C]_X$ is the cation concentration at X. Additionally, electrophoretic accumulation of cationic trackers in mitochondria is commonly enhanced by using lipophilic trackers and trackers which incorporate functional groups which covalently bind to mitochondrial proteins [S14,15].

In addition to being cationic, mitochondria trackers are commonly lipophilic [S15,16]. Since commonly used mitochondria targeting groups, such as triphenylphosphonium (TPP^+) possess a large hydrophobic surface and a large ionic radius ($r_0 \approx 4.2$ Å) due to the delocalization of the positive charge [S15–17], they can easily permeate the inner mitochondrial membrane and are adsorbed to its surfaces at the N and P sides, being distributed approximately according to eqn (S4) [S16].

Immobilizable mitochondria trackers that covalently bind to intramitochondrial proteins have been developed, allowing for the trackers to remain bound to mitochondria even in scenarios in which $\Delta\mu_{\mathsf{H}^+}$ vanishes as a result of pathological or toxicological conditions [S14,15]. Trackers of this type incorporate reactive functional groups, such as chloromethyl moieties that form covalent bioconjugates with thiol groups [S14,15,18,19] or aldehydes which bind to amino groups of mitochondrial proteins [S15,20,21].

It is worthwhile to note that some trackers, despite being cationic, accumulate in mitochondria regardless of the membrane polarization, i.e. in cases in which $\Delta\Psi_{\mathsf{NP}} = 0$ [S14]. This is achieved by targeting species unique to mitochondria, either by strong lipophilicity, ultimately resulting in electrostatic binding of the trackers to lipids specific to the mitochondrial inner membrane [S14,22–24] or by covalently binding to mitochondrial proteins [S14,25].

S6 Mitochondrial localization of neutral trackers

In contrast to cationic trackers, there have been far fewer reports of neutral tracking probes[S26–36] despite the significant advantage neutral trackers offer over charged ones. The physical mechanisms involved in the uptake of neutral dyes into mitochondria are not as well investigated as the ones for cationic dyes [S28,34], leading to design strategies frequently based on phenomenological observations. A generally accepted desired property of neutral trackers is the possession of a strong electron acceptor group, which results in a δ^+ character in a certain region of the molecular structure [S28,29,33], thereby enabling localization due to $\Delta\Psi_{\mathrm{NP}}$, analogously to cationic trackers. We are, however, not aware of any theoretical or experimental studies which investigate the extent of this effect.

A π-extension of 2,1,3-benzothiadiazole has been shown to lead to mitochondrial selectivity [S27]. A study of three BODIPY-based neutral trackers attributed their localization in mitochondria to the inclusion of the electron acceptor group CF_3 [S29]; however, one of the reported compounds localizes in mitochondria despite not including CF_3, calling into question the relevance of the assumed mechanism. Localization of an another class of BODIPY-based dyes was attributed to water soluble thio-hexose sugars linked to the BODIPYs [S31]. Trackers including nitrogen heterocycles with N-H bonds have been shown to localize in mitochondria [S32]; to the extent of our knowledge, the specific mechanism of localization has not yet been investigated. Compounds containing amides are suspected to target mitochondrial proteins and peptides [S34].

Considering the lack of a generally accepted basic physical picture of mitochondrial localization of neutral trackers, in this study we provide a critical assessment of various possible localization mechanisms of the considered candidate trackers (**FM** and **MOFM**), in an attempt to improve the framework for rational design of neutral trackers in future studies. In general, we assume that the cell membrane and the outer mitochondrial membrane are permeable to **FM** and **MOFM** [S37]; therefore, we consider localization to occur either within the inner membrane or the mitochondrial matrix.

S6.1 Localization due to (temporary) protonation

We consider the possibility of the trackers being protonated in the intermembrane space, thereby becoming positively charged and localizing in the mitochondrial matrix by exploiting $\Delta\Psi_{\mathrm{NP}}$. Such an effect has been shown to enhance mitochondrial localization of neutral thiophene based terpyridine trackers [S38]. However, measurements of the absorption spectra of **FM** and **MOFM** as a function of the environment acidity [S39] indicate that both trackers exhibit very low proton affinities in the conditions found in the intermembrane space (pH $\approx$ 7.0 - 7.4 [S40]), leading us to the conclusion that this localization mechanism is extremely unlikely in the cases of **FM** and **MOFM**.

S6.2 Covalent binding to species specific to mitochondria

As previously discussed, a number of cationic trackers are known to accumulate in mitochondria regardless of the polarization of the inner membrane by targeting species unique to mitochondria [S14]. Hence, it is conceivable that neutral trackers may accumulate in mitochondria due to the same mechanism. We consider this to be unfeasible in the case of **FM**, as it possesses no reactive functional groups which could form a covalent bond.

In the case of **MOFM**, we considered the possibility of O-demethylation occurring through promiscuous cytochromes, as a potential enzymatic replacement of the methoxy group with hydroxy would allow the molecule to be more reactive. It was found that cytochrome P450, an enzyme found in the inner mitochondrial membrane [S41] is an active chemical substrate for O-demethylation of lignine derivatives [S42]. We hypothesized that it could be an active site for a similar reaction to happen on **MOFM.** Our investigation of this physical mechanism is described in details in the section S8. Our results show that O-demethylation of **MOFM** is unlikely due to steric hinderance.

Table S7 Parameters obtained by fitting corresponding functional forms of the electrostatic potential (see text)

	k	0.21025391			
	x_0	-4.04551744			
Φ^0_{W}	A	3.02759882	Φ^0_{P}	A	1.80668022
	B	0.0536862		B	0.10159336
	k_1	0.52692898		k_1	0.5
	k_2	0.04830462		k_2	0.04044771
	x_1	-20.06043877		x_1	-18.81592035
F_{W}	C	-0.20836399	F_{P}	E	-0.180192605
	D	0.17272051		F	0.0815752725
	k_1^{W}	-0.2043405		α	0.924836054
	k_2^{W}	1.25557244		x_1^{P}	15.4943232
	x_1^{W}	14.75361901		k^{P}	$8.15226002 \cdot 10^{-4}$
	x_2^{W}	-21.70555879			

S7 Model of the electrostatic potential across the inner mitochondrial membrane

We model the inner mitochondrial membrane as a phospholipid bilayer surrounded by water. We consider the phospholipid bilayer to be consisting purely of palmitoyl-oleyl-phosphatidylcholine (POPC). The total electrostatic potential is given by:

$$\Phi(x, \Delta\Psi_{\mathsf{NP}}) = \Phi_{\mathsf{P}}(x, \Delta\Psi_{\mathsf{NP}}) + \Phi_{\mathsf{W}}(x, \Delta\Psi_{\mathsf{NP}}), \tag{S5}$$

where $\Phi_{\mathsf{P}}(x, \Delta\Psi_{\mathsf{NP}})$ is the electrostatic potential generated by the POPC bilayer and $\Phi_{\mathsf{W}}(x, \Delta\Psi_{\mathsf{NP}})$ is generated by water. $\Delta\Psi_{\mathsf{NP}}$ is a voltage drop across the membrane induced by an external homogenous electric field.

To fit a functional form of $\Phi(x, \Delta\Psi_{\mathsf{NP}})$, we use results from molecular dynamics (MD) simulations of the water-POPC bilayer system found in the literature [S43]. The extracted data and the obtained fitted curves are shown on Fig. S12. The data was extracted from Fig. 2(a) of Ref. [S43] using a data extraction tool [S44]. We use the following ansatz:

$$\begin{aligned} \Phi_{\mathsf{P}}(x, \Delta\Psi_{\mathsf{NP}}) &= \Phi^0_{\mathsf{P}}(x)\Big(1 + \Delta\Psi_{\mathsf{NP}} F_{\mathsf{P}}(x)\Big), \\ \Phi_{\mathsf{W}}(x, \Delta\Psi_{\mathsf{NP}}) &= \Phi^0_{\mathsf{W}}(x)\Big(1 + \Delta\Psi_{\mathsf{NP}} F_{\mathsf{W}}(x)\Big) + \frac{\Delta\Psi_{\mathsf{NP}}}{1 + e^{-k(x-x_0)}}, \end{aligned} \tag{S6}$$

where $\Phi^0_{\mathsf{P}}(x)$ and $\Phi^0_{\mathsf{W}}(x)$ are the electrostatic potentials of the POPC bilayer and water when $\Delta\Psi_{\mathsf{NP}} = 0$, $F_{\mathsf{P}}(x)$ and $F_{\mathsf{W}}(x)$ model the polarization of the subsystems in an external homogenous electric field and k and x_0 are free parameters of the logistic curve. We found that the following functional forms describe $\Phi^0_{\mathsf{W,P}}(x)$ well:

$$\Phi^0_{\mathsf{W,P}}(x) = \pm\Big(\frac{A}{1 + e^{-k_1(|x|-x_1)}} - B|x|e^{-k_2(|x|-x_1)^2}\Big), \tag{S7}$$

where A, B, k_1, k_2 and x_1 are free parameters and the plus and minus signs are chosen for $\Phi^0_{\mathsf{W}}(x)$ and $\Phi^0_{\mathsf{P}}(x)$ respectively, with $A, B > 0$. The fit is shown on Fig. S12 on the left and the obtained parameters are given in Table S7. For $F_{\mathsf{W}}(x)$ and $F_{\mathsf{P}}(x)$ we fit the following functional forms:

$$\begin{aligned} F_{\mathsf{W}}(x) &= -\Big(\frac{C}{1 + e^{-k_1^{\mathsf{W}}(x - x_1^{\mathsf{W}})}} + \frac{D}{1 + e^{-k_2^{\mathsf{W}}(x - x_2^{\mathsf{W}})}}\Big), \\ F_{\mathsf{P}}(x) &= E + F\tanh\Big(\alpha(x - x_1^{\mathsf{P}})\Big)\tanh\Big(\alpha(x + x_1^{\mathsf{P}})\Big)e^{-k^{\mathsf{P}}x^2}, \end{aligned} \tag{S8}$$

where $C, D, E, F, k_i^{\mathsf{W,P}}, x_i^{\mathsf{W,P}}$ and α_i $(i = 1, 2)$ are free parameters. The obtained fit for $\Delta\Psi_{\mathsf{NP}} = -0.8$ is shown in the right panel of Fig. S12.

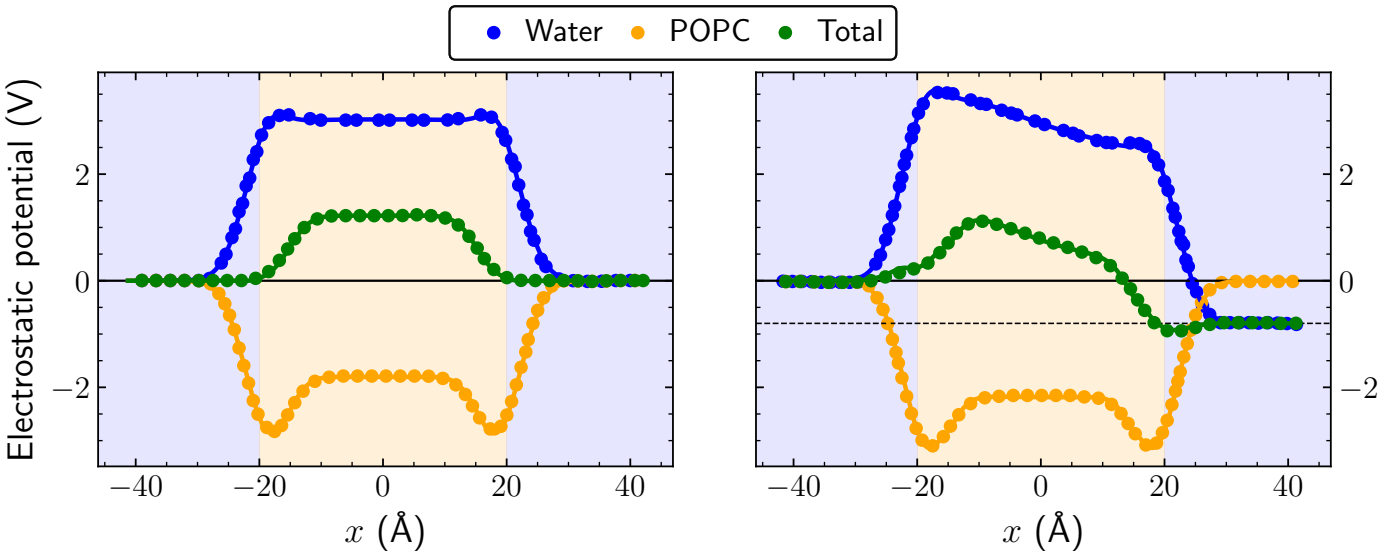

Figure S12 Data used for fitting the electrostatic potential across across the inner mitochondrial membrane (scatter points) and the obtained fitted curves (full lines), shown for $\Delta\Psi_{\mathrm{NP}} = 0.0$ V (left panel) and $\Delta\Psi_{\mathrm{NP}} = -0.8$ V (right panel). The "Total" fitted curve is calculated as a sum of "Water" and "POPC" fitted curves. The region containing predominantly water (POPC) is highlighted by the light blue (orange) background.

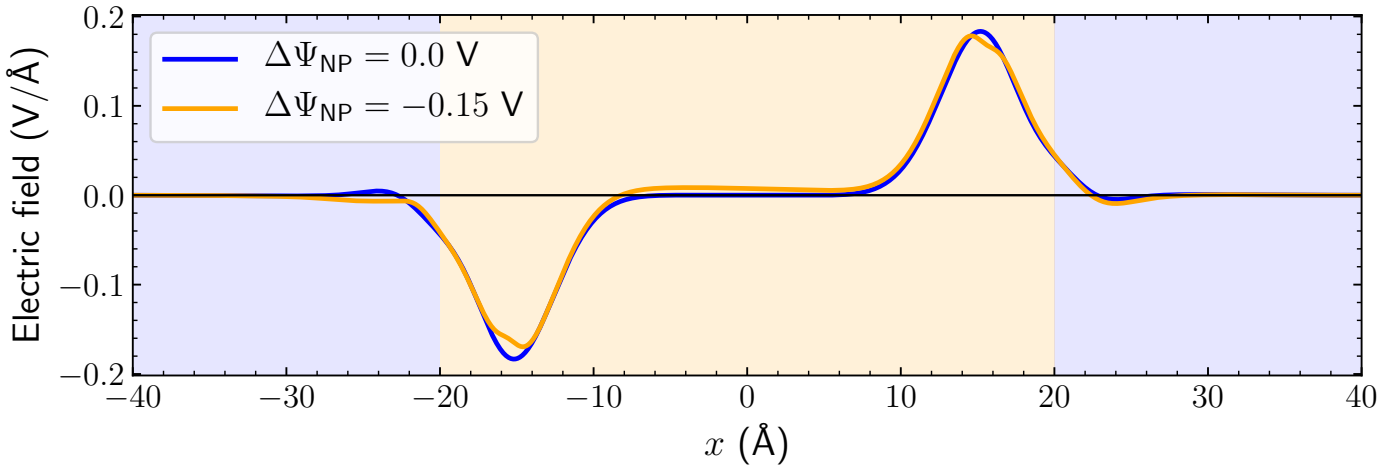

Figure S13 Electric field across the inner mitochondrial membrane for $\Delta\Psi_{\mathrm{NP}} = 0.0$ V and $\Delta\Psi_{\mathrm{NP}} = -0.15$ V. The region containing predominantly water (POPC) is highlighted by the light blue (orange) background.

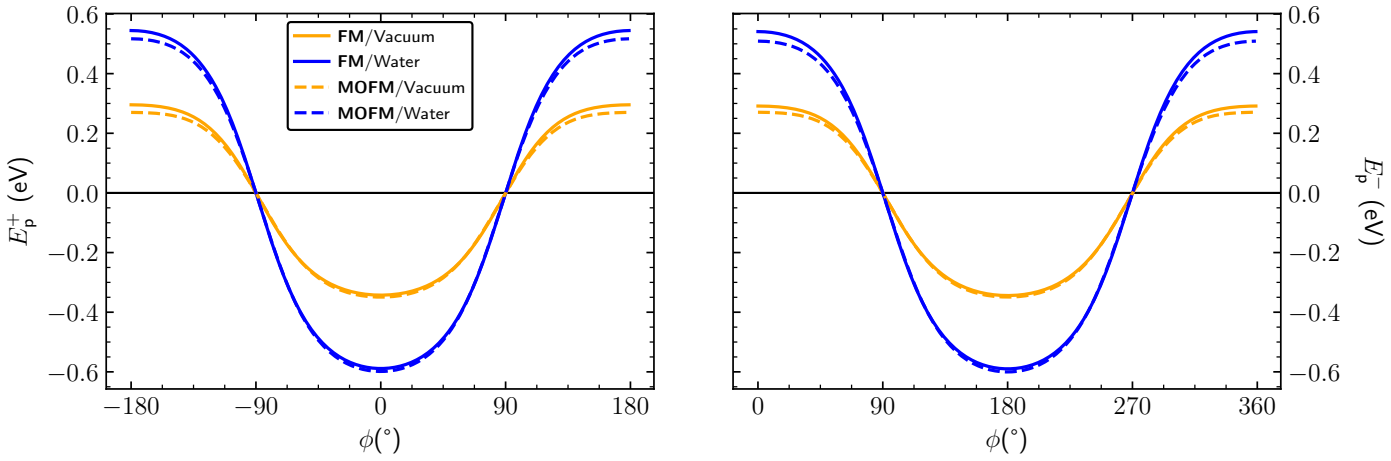

Figure S14 Electrostatic potential energy as a function of the angle between the molecular dipole moment and the x-axis, calculated using Mulliken charges in different solvents (vacuum, DMSO and water) with the position of the molecular center of mass x fixed at the binding sites (see main text), i.e. the position x at which $E^{\pm}(x)$ is minimal.

S8 MD and docking simulations of MOFM in cythochrome P450

Besides the physical mechanism proposed in the main, we also hypothesized that a further degree of localization could be induced by the possibility of the dyes to undergo bio-chemical reactions in the mitochondrial space. Being inspired by an extensive work on promiscuous cytochromes able to participate in aromatic catabolism[S42], we have run molecular dynamics simulations on such model P450 featuring "open states" and explore its docking by **MOFM**. In this work[S42], the "open state" of a P450 cythocrome has been proven both experimentally and computationally to allow first molecule binding and then de-methoxylation reaction of lignin derivatives .

The possibility of **MOFM** to dock this promiscuous P450 cythocrome through molecular dynamics and docking simulations, was not successfull, i.e. we did not find any relevant docking sites, main reason being the steric hindrance of **MOFM** dye. However, we cannot conclude that investigate dyes would not bind to any promiscuous cythochromes.

S8.1 Computational model building

The models of the P450 cythochrome were based on the X-ray structure of 5NCB in apo- state as deposited in the protein data bank (PDB code: 5NCB) [S42]. The protonation state was selected according to the same work - which in turn was determined employing H++ [S45]. Topologies for all studied systems were generated using the tleap module of AmberTools20 [S46]. The FF14SB AMBER force field (FF) [S47] was used for the protein. As suggested, special care had to be taken to parametrize the Fe atom contained in the structure, following a previously reported parametrization [S48]. The MOFM parameters were derived from the Gaff FF [S46]. To derive the ESP charges of MOFM, we computed its electrostatic potential [S49] by performing geometry optimization at the Hartree-Fock level of theory with a 6-31G* basis set using the Gaussian09 software. These were then converted to RESP charges with the Antechamber module of Ambertools22. The model system was neutralized by adding Na+ ions, which were then described with the the parameters of Joung and Cheatham [S50]. A layer of 14 Å from the solute boundary of TIP3P water molecules [S51] has been added to all systems, leading to a total system size of 86000 atoms. Subsequently, the topologies were converted to the GROMACS format using the parmed software [S52].

S8.2 Molecular dynamics and docking computational details

Classical MD simulations of 5NCB-apo were done with the GROMACS 2020.6 code [S53]. An integration time step of 2 fs was used, and all covalent bonds involving the hydrogen atoms were constrained with the LINCS algorithm [S54]. We used the Particle Mesh Ewald scheme to account for electrostatic interactions [S55], using a real space cut-off of 10 Å. MD simulations were performed in the isothermal-isobaric NPT ensemble at a temperature of 300 K, under the control of the velocity-rescaling thermostat [S56] and the Parrinello-Rahman barostat [S57]. Preliminary energy minimization was performed by employing the steepest descent algorithm. Subsequently, we gradually heated the system to 300 K with an increase of 50 K every 2 ns for a total of 12 ns, keeping the entire system highly restrained except for the solvent atoms and the solute hydrogens. Then we switched to the NPT ensemble, scaling the pressure to 1 bar and using two different barostats: (i) the Berendsen barostat was used for 20 ns with the same restraints on the solute atoms, and (ii) the Parrinello-Rahman barostat for 30 additional ns while leaving the side chains free of restraints. Next, we gradually decreased the restraints in 20 ns. Finally, all systems were simulated for 2 μs of MD simulation. We have collected a total of 5 replicas. Since the cythocrome is known to visit and open and a closed conformation, we have defined a collective variable able to track these two states. This was done following the original work [S42], we have employed the root-mean-square deviation (RMSD) of the C_α atoms of residues #150-#206, corresponding to the two helices responsible for the opening of the cytochrome. By this analysis, we were able to identify frames, across the all 5 trajectories, corresponding to “open state”, which were associated to a RMSD value larger than 0.2 nm. This analysis, performed with the GROMACS 2020.6 program, was done to detect the structures of the cytochrome exhibiting the largest opening of the active site. These 2 structure were then used as 5NCB-apo target for docking simulations of MOFM. In addition, we also candidate the 2 most-representative structures selected from the MD trajectories corresponding to open state. Such representative structure was selected through RMSD-clustering of the AmberTool cpptraj. Docking simulations of 5NCB/MOFM were performed using the extra-precision protocol from Glide software of the Schrödinger suite [S58], release 2021-4, with Maestro Version 13.0.137. In the attempt of docking MOFM on these 4 structures, we used a van der Waals (vdW) radius scaling factor of 0.80 Å for protein and ligand atoms with a partial charge of less than 0.15 to mimic protein flexibility.

Notes and references

[S1] F. Neese, *WIREs Computational Molecular Science*, 2022, **12**, e1606.

[S2] C. Adamo and V. Barone, *The Journal of Chemical Physics*, 1999, **110**, 6158–6170.

[S3] F. Weigend and R. Ahlrichs, *Phys. Chem. Chem. Phys.*, 2005, **7**, 3297–3305.

[S4] F. Weigend, *Phys. Chem. Chem. Phys.*, 2006, **8**, 1057–1065.

[S5] A. V. Marenich, C. J. Cramer and D. G. Truhlar, *The Journal of Physical Chemistry B*, 2009, **113**, 6378–6396.

[S6] K. Swathi, M. Sujith, P. Divya, A. Delledonne, D. A. P. Huu, F. Di Maiolo, F. Terenziani, A. Lapini, A. Painelli, C. Sissa *et al.*, *Chemical Science*, 2023, **14**, 1986–1996.

[S7] F. Bertocchi, A. Delledonne, G. Vargas-Nadal, F. Terenziani, A. Painelli and C. Sissa, *The Journal of Physical Chemistry C*.

[S8] M. A. Albota, C. Xu and W. W. Webb, *Applied Optics*, 1998, **37**, 7352–7356.

[S9] S. de Reguardati, J. Pahapill, A. Mikhailov, Y. Stepanenko and A. Rebane, *Optics Express*, 2016, **24**, 9053–9066.

[S10] L. D. Zorova, V. A. Popkov, E. Y. Plotnikov, D. N. Silachev, I. B. Pevzner, S. S. Jankauskas, V. A. Babenko, S. D. Zorov, A. V. Balakireva, M. Juhaszova *et al.*, *Analytical biochemistry*, 2018, **552**, 50–59.

[S11] S. W. Perry, J. P. Norman, J. Barbieri, E. B. Brown and H. A. Gelbard, *Biotechniques*, 2011, **50**, 98–115.

[S12] B. Kadenbach, R. Ramzan, L. Wen and S. Vogt, *Biochimica et Biophysica Acta (BBA)-General Subjects*, 2010, **1800**, 205–212.

[S13] R. J. Ritchie, *Progress in biophysics and molecular biology*, 1984, **43**, 1–32.

[S14] C. Cottet-Rousselle, X. Ronot, X. Leverve and J.-F. Mayol, *Cytometry Part A*, 2011, **79**, 405–425.

[S15] X. Zhang, Q. Sun, Z. Huang, L. Huang and Y. Xiao, *Journal of Materials Chemistry B*, 2019, **7**, 2749–2758.

[S16] M. F. Ross, G. Kelso, F. H. Blaikie, A. M. James, H. M. Cocheme, A. Filipovska, T. Da Ros, T. Hurd, R. A. Smith and M. P. Murphy, *Biochemistry (Moscow)*, 2005, **70**, 222–230.

[S17] C. A. Kulkarni, B. D. Fink, B. E. Gibbs, P. R. Chheda, M. Wu, W. I. Sivitz and R. J. Kerns, *Journal of medicinal chemistry*, 2021, **64**, 662–676.

[S18] B. Chazotte, *Cold Spring Harb Protoc*, 2011, **2011**, 990–2.

[S19] S. Wu, Y. Song, Z. Li, Z. Wu, J. Han and S. Han, *Analytical Methods*, 2012, **4**, 1699–1703.

[S20] B. Wang, X. Zhang, C. Wang, L. Chen, Y. Xiao and Y. Pang, *Analyst*, 2015, **140**, 5488–5494.

[S21] X. Song, N. Li, C. Wang and Y. Xiao, *Journal of Materials Chemistry B*, 2017, **5**, 360–368.

[S22] A. Maftah, J. M. Petit and R. Julien, *FEBS letters*, 1990, **260**, 236–240.

[S23] A. Maftah, J. M. Petit, M.-H. Ratinaud and R. Julien, *Biochemical and biophysical research communications*, 1989, **164**, 185–190.

[S24] J.-M. Petit, A. Maftah, M.-H. Ratinaud and R. Julien, *European Journal of Biochemistry*, 1992, **209**, 267–273.

[S25] A. D. Presley, K. M. Fuller and E. A. Arriaga, *Journal of Chromatography B*, 2003, **793**, 141–150.

[S26] J. Jose, A. Loudet, Y. Ueno, R. Barhoumi, R. C. Burghardt and K. Burgess, *Organic & biomolecular chemistry*, 2010, **8**, 2052–2059.

[S27] B. A. D Neto, J. R. Corrêa, P. H. Carvalho, D. C. Santos, B. C. Guido, C. C. Gatto, H. C. de Oliveira, M. Fasciotti, M. N. Eberlin and E. N. d. Silva Jr, *Journal of the Brazilian Chemical Society*, 2012, **23**, 770–781.

[S28] B. A. Neto, J. R. Corrêa and R. G. Silva, *RSC advances*, 2013, **3**, 5291–5301.

[S29] T. Gayathri, S. Karnewar, S. Kotamraju and S. P. Singh, *ACS Medicinal Chemistry Letters*, 2018, **9**, 618–622.

[S30] H. Yao, G. Wei, Y. Liu, H. Yao, Z. Zhu, W. Ye, X. Wu, J. Xu and S. Xu, *ACS Medicinal Chemistry Letters*, 2018, **9**, 1030–1034.

[S31] P. E. Kesavan, V. Pandey, M. K. Raza, S. Mori and I. Gupta, *Bioorganic Chemistry*, 2019, **91**, 103139.

[S32] Y. Wang, B. Xu, R. Sun, Y.-J. Xu and J.-F. Ge, *Journal of Materials Chemistry B*, 2020, **8**, 7466–7474.

[S33] Á. Ramos-Torres, E. Avellanal-Zaballa, F. García-Garrido, A. B. Fernández-Martínez, A. Prieto-Castaneda, A. R. Agarrabeitia, J. Bañuelos, I. García-Moreno, F.-J. Lucio-Cazana and M. J. Ortiz, *Chemical Communications*, 2021, **57**, 5318–5321.

[S34] W. Ma, B. Xu, R. Sun, Y.-J. Xu and J.-F. Ge, *Journal of Materials Chemistry B*, 2021, **9**, 2524–2531.

[S35] B. Roy, M. C. Reddy, G. P. Jose, F. C. Niemeyer, J. Voskuhl and P. Hazra, *The Journal of Physical Chemistry Letters*, 2021, **12**, 1162–1168.

[S36] H. G. Agrawal, P. S. Giri, P. Meena, S. N. Rath and A. K. Mishra, *ACS Medicinal Chemistry Letters*, 2023.

[S37] J. J. Lemasters, *Journal of gastroenterology and hepatology*, 2007, **22**, S31–S37.

[S38] X. Tian, Y. Zhu, M. Zhang, J. Tan, Q. Zhang, X. Wang, J. Yang, H. Zhou, J. Wu and Y. Tian, *Dyes and Pigments*, 2017, **139**, 431–439.

[S39] K. V. Vygranenko, Y. M. Poronik, A. Wrzosek, A. Szewczyk and D. T. Gryko, *Chemical Communications*, 2021, **57**, 7782–7785.

[S40] A. M. Porcelli, A. Ghelli, C. Zanna, P. Pinton, R. Rizzuto and M. Rugolo, *Biochemical and biophysical research communications*, 2005, **326**, 799–804.

[S41] K. Berka, T. Hendrychová, P. Anzenbacher and M. Otyepka, *The journal of physical chemistry A*, 2011, **115**, 11248–11255.

[S42] S. J. B. Mallinson, M. M. Machovina, R. L. Silveira, M. Garcia-Borràs, N. Gallup, C. W. Johnson, M. D. Allen, M. S. Skaf, M. F. Crowley, E. L. Neidle, K. N. Houk, G. T. Beckham, J. L. DuBois and J. E. McGeehan, *Nature Communications*, 2018, **9**, 2487.

[S43] L. Delemotte and M. Tarek, *The Journal of membrane biology*, 2012, **245**, 531–543.

[S44] *AutoMeris WebPlotDigitizer*, Available on `https://apps.automeris.io/wpd/`. Accessed on 11/24/2023.

[S45] J. C. Gordon, J. B. Myers, T. Folta, V. Shoja, L. S. Heath and A. Onufriev, *Nucleic Acids Research*, 2005, **33**, W368–W371.

[S46] *Amber 2020*, 2020, University of California, San Francisco.

[S47] J. A. Maier, C. Martinez, K. Kasavajhala, L. Wickstrom, K. E. Hauser and C. Simmerling, *Journal of Chemical Theory and Computation*, 2015, **11**, 3696–3713.

[S48] K. Shahrokh, A. Orendt, G. S. Yost and T. E. Cheatham III, *Journal of Computational Chemistry*, 2012, **33**, 119–133.

[S49] C. I. Bayly, P. Cieplak, W. Cornell and P. A. Kollman, *The Journal of Physical Chemistry*, 1993, **97**, 10269–10280.

[S50] I. S. Joung and T. E. I. Cheatham, *The Journal of Physical Chemistry B*, 2008, **112**, 9020–9041.

[S51] W. L. Jorgensen, J. Chandrasekhar, J. D. Madura, R. W. Impey and M. L. Klein, *The Journal of Chemical Physics*, 1983, **79**, 926–935.

[S52] M. R. Shirts, C. Klein, J. M. Swails, J. Yin, M. K. Gilson, D. L. Mobley, D. A. Case and E. D. Zhong, *bioRxiv*, 2016.

[S53] M. J. Abraham, T. Murtola, R. Schulz, S. Páll, J. C. Smith, B. Hess and E. Lindahl, *SoftwareX*, 2015, **1-2**, 19–25.

[S54] B. Hess, H. Bekker, H. J. C. Berendsen and J. G. E. M. Fraaije, *Journal of Computational Chemistry*, 1997, **18**, 1463–1472.

[S55] T. Darden, D. York and L. Pedersen, *The Journal of Chemical Physics*, 1993, **98**, 10089–10092.

[S56] G. Bussi, D. Donadio and M. Parrinello, *The Journal of Chemical Physics*, 2007, **126**, 014101.

[S57] M. Parrinello and A. Rahman, *Journal of Applied Physics*, 1981, **52**, 7182–7190.

[S58] R. A. Friesner, J. L. Banks, R. B. Murphy, T. A. Halgren, J. J. Klicic, D. T. Mainz, M. P. Repasky, E. H. Knoll, M. Shelley, J. K. Perry, D. E. Shaw, P. Francis and P. S. Shenkin, *Journal of Medicinal Chemistry*, 2004, **47**, 1739–1749.